Plasma Phys. Control. Fusion **51** (2009) 014007 (11pp) doi:10.1088/0741-3335/51/1/014007

Experimental investigation of fast electron transport through Kα imaging and spectroscopy in relativistic laser–solid interactions

P Köster[1,2,8], K Akli[3], D Batani[4], S Baton[5], R G Evans[6,7], A Giulietti[1,2], D Giulietti[1,2,8], L A Gizzi[1,2], J S Green[6,7], M Koenig[5], L Labate[1,2], A Morace[4], P Norreys[7], F Perez[5], J Waugh[9], N Woolsey[9] and K L Lancaster[7]

[1] Intense Laser Irradiation Laboratory - IPCF, Consiglio Nazionale delle Ricerche, via Moruzzi 1, 56124 Pisa, Italy
[2] INFN, Sezione di Pisa, Largo B. Pontecorvo 3, 56127 Pisa, Italy
[3] Department of Physics, Ohio State University, Columbus, Ohio 43200-1117, USA
[4] Dipartmento di Fisica 'G. Occhialini', Università di Milano Bicocca, Piazza della Scienza 3, 20126 Milano, Italy
[5] Laboratoire Pour I'Utilisation des Lasers Intenses, Ecole Polytechnique, CNRS, 91128 Palaiseau, France
[6] Blackett Laboratory, Imperial College London, Prince Consort Road, London SW1 2BZ, UK
[7] Central Laser Facility, Rutherford Appleton Laboratory, Chilton, Didcot, Oxon, OX11 OQX, UK
[8] Dipartimento di Fisica, Università di Pisa, Largo B. Pontecorvo 3, 56127 Pisa, Italy
[9] Department of Physics, University of York, Heslington, Y010 5DD, UK

Received 7 July 2008, in final form 15 October 2008
Published 9 December 2008
Online at stacks.iop.org/PPCF/51/014007

Abstract

We report on experimental fast electron transport studies performed in the relativistic laser intensity interaction regime. The investigation has been carried out in the long-pulse (0.6 ps) regime relevant for the fast ignitor scheme in the inertial confinement fusion concept.

Multilayer targets containing different materials were irradiated. Here we show the results concerning SiO_2 or Al layers, respectively. The Kα radiation from a Cu tracer layer on the target rear side was found to be enhanced by a factor of about 8 with the irradiation of SiO_2 targets with respect to the Al targets. The possible origin of this observation is discussed.

(Some figures in this article are in colour only in the electronic version)

1. Introduction

During the interaction of high-intensity short laser pulses with solid targets a copious amount of electrons with kinetic energy significantly higher (hundreds of kiloelectronvolts up to

megaelectronvolts) than the mean electron energy (tens or hundreds of electronvolts) are generated. The generation of these so-called 'fast' or 'hot' electrons and their propagation in matter have been studied extensively for many years both experimentally and theoretically. The laser–matter interaction [1] and the electron transport dynamics [2, 3] have been investigated numerically and analytically, including the influence of different plasma density scalelengths on the laser absorption and fast electron temperature [4] and the effects of self-generated magnetic and electric fields on the transport dynamics [5–9], with particular attention to the resistivity of the target material [10, 11]. From an experimental point of view, mainly x-ray measurements were employed as diagnostic techniques [12–20], but also direct measurements of the forward escaping electrons [21, 22], shadowgraphy [23, 24] and optical emission from the rear surface are used [25, 26].

The study of fast electron transport phenomena is of interest for the development of proton sources [27] and ultrafast x-ray sources [28] as well as for the study of matter in extreme conditions, such as measurements of the equation of state and the opacity of high pressure material relevant to astrophysics [29].

Moreover, the detailed knowledge of the fast electron generation and transport mechanisms is of a fundamental importance for the fast ignition (FI) approach to inertial confinement fusion, which is the main goal of the programme of the High Power laser Energy Research Facility (HiPER) presently under preparation in Europe. In the FI scheme an ultra-high current of relativistic electrons has to propagate through an outer low Z plasma layer in order to deposit the energy of the electrons in the core of the fusion pellet, creating a hot spot and thus igniting the fuel [30, 31].

The forward propagating fast electrons produced during the laser–matter interaction enter the underlying target material, where they deposit their kinetic energy partially or entirely through different physical mechanisms including collisions with the target atoms or ions, electric and magnetic field generation. In particular x-ray fluorescence, the so-called Kα lines, characteristic of the target material, are generated via collisional inner-shell ionization of the target atoms and subsequent radiative decay.

A typical experimental approach to the study of fast electron transport is the irradiation of multilayer target foils [16]. The targets consist of at least two layers of solid material of a different atomic number. The first layer is the propagation layer, made of the material in which the transport of the fast electrons is to be studied. Often the thickness of the propagation layer and/or the material is varied in the experiment. The second layer is the tracer layer which is made of a material suitable for the x-ray fluorescence measurements.

In addition to the x-ray measurements, direct measurements of the electrons leaving the target foil and optical transition radiation measurements are often employed. Also, the laser–solid interaction conditions, as well as the target rear side dynamics may be characterized by interferometric and/or optical scattering measurements.

The experiment described in this report was designed for a systematic study of fast electron energy transport in different target materials for high-intensity, long-pulse interaction conditions that are of interest for the FI case. In particular, the relatively long-pulse duration (0.6 ps) allows the investigation of effects which occur on a time-scales not accessible in femtosecond laser–matter interactions. In the experiment, metallic and dielectric targets with similar atomic number Z were irradiated in order to distinguish between effects arising due to different atomic numbers Z and those dependent on the target conductivity. Although in full-scale FI, the target resistivity is less important than in nowadays experiments, as the FI beam interacts with a preformed plasma, the detailed understanding of the physical processes involved in fast electron transport is fundamental in order to reduce uncertainties in the design of FI.

2. Objectives of the experiment and target choice

The idea of the experiment was the investigation of the transport of the energetic electrons generated during the laser–matter interaction in the target material, with particular attention to differences of the electron transport in conducting/dielectric materials with similar atomic number Z.

Therefore, sets of multilayer targets containing a metallic (Al), a dielectric (SiO_2) layer, respectively, have been used. The targets consisted of two layers each. The laser-irradiated layer was made of Al or SiO_2 of two different thicknesses (25 or 50 μm), while the second layer, that is, the so-called tracer layer, consisted of 1 μm thick Cu. The transverse dimensions of these targets were some mm^2.

3. Experimental setup

The experiment described here was carried out with the VULCAN Petwatt beam at the Rutherford Appleton Laboratory. The laser pulse (wavelength $\lambda = 1.054\,\mu$m) had a duration of 600 fs and an energy per pulse of 700 J. The contrast of the laser pulse is about 10^{-8} at 2 ns and 10^{-9} at 10 ns before the peak of the main laser pulse. Throughout the experiment a pulse energy of 440 J (measured before the compressor gratings) was used in order to reduce the noise on the diagnostic devices. This noise arises from energetic electrons and secondary x-rays emitted from the materials inside the target chamber. The laser beam was focused by means of an $f/3$ off-axis parabolic mirror on the target surface. 30% of the energy was contained in a moderately elliptical focal spot of $6 \times 4\,\mu m^2$ size. The average intensity in the focal spot is therefore about $6 \times 10^{20}\,W\,cm^{-2}$. In reality, as will be discussed later, the fast electron temperature derived from the average intensity is overestimated and the actual intensity distribution should be used to calculate the fast electron distribution [32]. A more detailed calculation of the local fast electron temperature taking into account the laser intensity distribution is in progress.

Two x-ray pinhole cameras equipped with Imaging Plate (Fujifilm BAS-SR 2040) detectors were mounted to look at either side of the target surface. An Al foil was used to stop visible and infrared radiation. The pinhole diameter was 5 μm and the magnification was 12.3 ± 0.4 for the front pinhole camera and 11.5 ± 0.4 for the back pinhole camera.

A spherically bent quartz crystal was used to perform 2D imaging of the Cu Kα emission. The spatial resolution of the images was about 10 μm and the magnification was 17.4. The same spectral range, that is, the x-ray radiation around 8 keV was spectrally resolved by the use of a spherically bent mica crystal in FSSR-1D configuration working in the 11th order of diffraction. Both these diagnostics were equipped with imaging plates for the detection of the x-rays.

4. Experimental results

In this section we describe some preliminary results from the interaction of the laser pulse with the targets containing an SiO_2 or Al propagation layer. In particular, we focus our attention to the x-ray measurements including pinhole camera images and high resolution x-ray spectra obtained with the bent mica crystal spectrometer.

In figures 1 and 2, the pinhole camera images obtained from the interaction of the laser pulse with a 50 μm SiO_2 + 1 μm Cu back layer target are shown.

Figures 1 and 2 show the raw data for the front (the one looking from the laser-irradiated side) and the back pinhole camera, respectively. After calculation of the centre-of-mass of

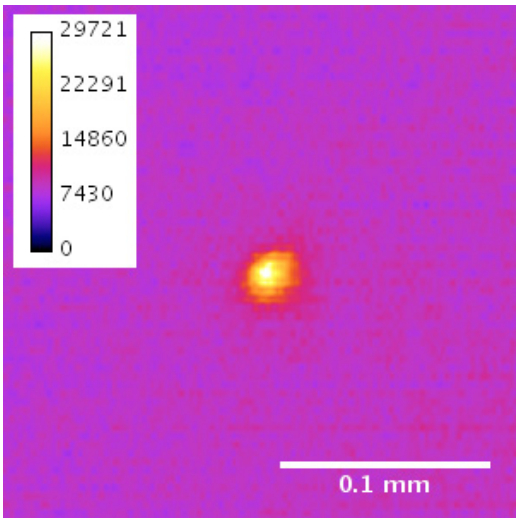

Figure 1. Front pinhole camera image of the x-ray emission from the interaction of the laser pulse with a layered target consisting of a 50 μm thick SiO_2 front layer and a 1 μm thick Cu back layer.

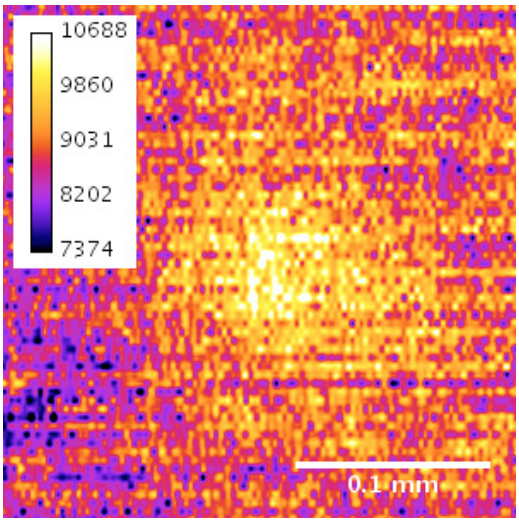

Figure 2. Back pinhole camera image of the x-ray emission from the interaction of the laser pulse with a layered target consisting of a 50 μm thick SiO_2 front layer and a 1 μm thick Cu back layer.

the x-ray emission region, the average intensity over the circle was calculated for each radial distance from the centre in 10 μm steps. The radial lineouts obtained in this way are displayed together with a Guassian fit in figures 3 and 4, respectively. The front pinhole camera image shows an x-ray source of about 16 μm FWHM diameter size, whereas the x-ray source seen with the back pinhole camera has a diameter of 81 μm FWHM. The background subtracted peak intensity of the emission is more than an order of magnitude less on the back pinhole camera with respect to the front pinhole camera.

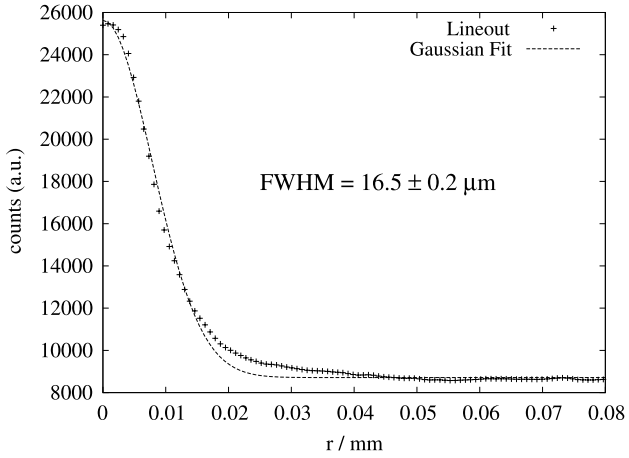

Figure 3. Radial lineout of figure 1 with Gaussian fit.

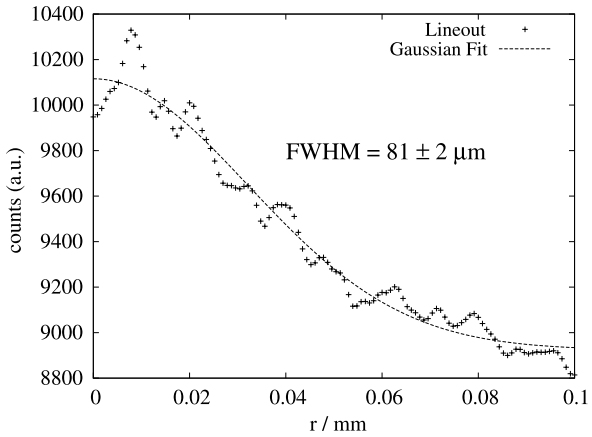

Figure 4. Radial lineout of figure 2 with Gaussian fit.

Similar pinhole camera images were obtained with irradiation of targets with Al propagation layers. In these circumstances the front pinhole camera images have a peak intensity of about one order of magnitude less than the one shown for the target with the SiO_2 propagation layer (figure 3), whereas the back pinhole camera images have similar peak intensities for the SiO_2 and the Al targets. The source size seen by the front pinhole camera is similar for both target types. From the analysis of the back pinhole camera images, the source size obtained for the Al containing targets is around 30 μm, which is much smaller than the x-ray source size observed with the irradiaiton of targets with SiO_2 propagation layer.

In figure 5 the x-ray emission spectrum around 8 keV is displayed. The spectrum was obtained from the irradiation of a target with a 50 μm thick SiO_2 propagation layer. The high background signal visible in the raw spectrum is due to noise arising from charged particles and x-rays emitted in such high-intensity laser–solid experiments, whereas the vertical streak-like pattern visible in figure 6 is mainly due to the read-out process of the imaging plate. The emission lines visible in the spectrum are the Kα_1 at 1.5406 Å (8.048 keV) and the Kα_2 at 1.5444 Å (8.028 keV) originating from the copper back layer. The intensity ratio of the

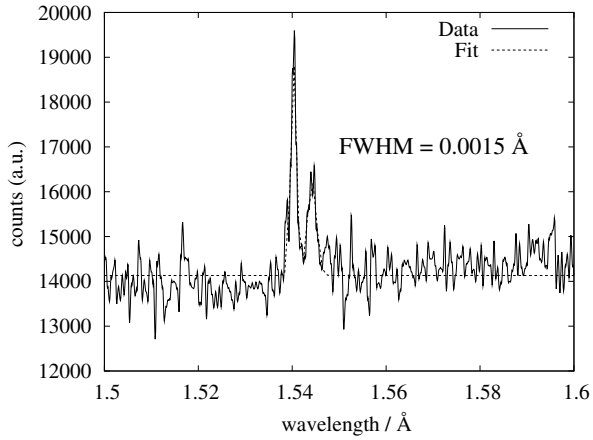

Figure 5. Lineout of the x-ray emission spectrum around the Kα line of Cu from the irradiation of a 50 μm SiO_2 + 1 μm Cu target at an intensity of about 5×10^{20} W cm^{-2}.

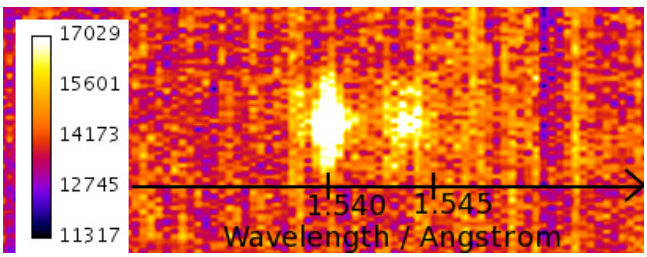

Figure 6. Raw data x-ray emission spectrum around the Kα line of Cu from the irradiation of a 50 μm SiO_2 + 1 μm Cu target at an intensity of about 5×10^{20} W cm^{-2}.

two components is about $I_{\alpha 2}/I_{\alpha 1} = 1/2$ as expected [33]. No continuous radiation has been observed in the whole spectral range diffracted from the crystal, as is clearly visible from figure 6.

The Kα_1 line was fitted with a Gaussian function in order to determine an upper limit for the spectral resolution of the bent crystal spectrometer in our experimental configuration. The FWHM of the Gaussian function is 1.5×10^{-3} Å, which results in a spectral resolution of the x-ray spectrometer $\lambda/\Delta\lambda$ better than 1000.

The Kα emission from the irradiation of the targets containing the Al propagation layer was generally below the detection threshold of the x-ray spectrometer, whereas very bright Kα lines have been detected for some data shots on targets containing a SiO_2 propagation layer. Other data shots on SiO_2 targets showed no Kα emission on the bent crystal spectrometer. These data shots are not considered in the following, as the x-ray emission detected with the pinhole cameras for these shots was hardly above the noise level showing structured emission with more than one intensity maximum, thus leading us to the conclusion that no proper interaction has taken place (possibly due to the target surface imperfections or to uncontrolled laser beam defects).

The Kα emission intensity was measured from the monochromatic images obtained with the 2D x-ray imaging crystal. In the cases of the targets with the SiO_2 propagation layer, the intensity of the Kα line was found to be higher by a factor of about 8 with respect to the images

obtained with the Al targets. The size of the emission region was similar for all experimental shots and was around 70 μm ($\pm$10 μm) for all detected signals.

5. Discussion

In the previous section experimental data from the irradiation of targets having a dielectric (SiO_2) and those having a metallic (Al) front layer were presented. The main difference observed for the two target types is the enhancement by a factor of about 8 of the Kα radiation emitted from the Cu tracer layer in the case of the targets with the SiO_2 propagation layer and a different x-ray source size observed with the back pinhole cameras for the two propagation layer materials (Al and SiO_2). We will now discuss these experimental results.

The front pinhole camera images show a similar x-ray source size for the two different target materials. The observed radiation is mainly due to plasma emission. The x-ray photon energies of the plasma emission are expected to be a few kiloelectronvolts, e.g. for a plasma electron temperature of 1.5 keV bremsstrahlung emission peaks around 3 keV [34]. These x-rays will be attenuated to a level below the detection threshold of the back pinhole camera by the target material itself, as the transmission for radiation up to 4 keV is at most a few per cent. Therefore the contribution of the plasma emission to the back pinhole camera images is negligible.

The radiation detected by the back pinhole camera can be attributed to Kα radiation and bremsstrahlung emission from collisions of the fast electrons with the target atoms. Bremsstrahlung from electrons with relativistic energies is emitted in the direction of the fast electron beam in a cone with aperture $1/\gamma$, where γ is the relativistic Lorentz factor of the fast electrons [35]. In the case of the target with the Al propagation layer, bremsstrahlung emission is dominant in the pinhole camera image, whereas the bright Kα emission from the Cu tracer layer of the target with the SiO_2 propagation layer gives a significant contribution to the back pinhole camera image. In fact, the measured source size of 81 μm is in agreement with the Kα source size measured with the 2D imaging crystal ($\simeq$80 μm).

Kα radiation is generated by inner-shell ionization of the target atoms and successive radiative decay of the atom in the excited state. In a simple manner the number of Kα photons emitted in the process can be written as

$$n_{\mathrm{K}\alpha} = n_{\mathrm{e}^-,\mathrm{fast}}\eta_{\mathrm{K}} \int \sigma(E) f(E)\,\mathrm{d}E, \tag{1}$$

where $n_{\mathrm{e}^-,\mathrm{fast}}$ indicates the number density of fast electrons, $\sigma(E)$ is the total cross section of K shell ionization as a function of the fast electron energy, $f(E)$ is the fast electron distribution function normalized to unity and η_{K} is the fluorescence yield. In the approximation that the ionization cross section and the fluorescence yield are material constants, the Kα yield can differ due to a different number of fast electrons or due to a different energy distribution of the fast electrons. As the K shell ionization cross section depends on the energy of the incoming electron, a different fast electron temperature leads to differences in the Kα yield. In order to illustrate this fact, in figure 7 the K shell ionization cross section is shown as a function of the incoming electron energy. The graph exhibits a maximum around a few tens of kiloelectronvolts. For higher energies the cross section decreases, having a minimum at around 1 MeV. For even higher, relativistic energies, the K shell ionization cross section increases again.

Since the fast electron distribution function could not be measured directly in the experiment, we use the temperature of the initial fast electron population derived from the

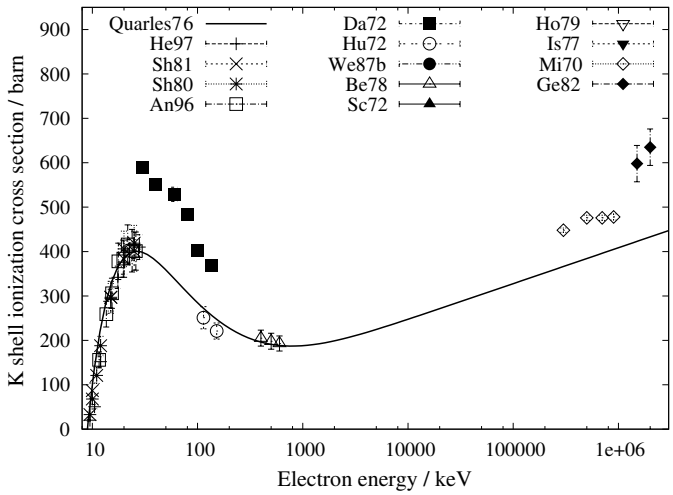

Figure 7. K shell ionization cross section in barn for copper as a function of the incoming electron energy in kiloelectronvolts. The experimental data points have been taken from [36] maintaining the same labeling for references therein. The theoretical curve has been plotted according to the formula given by Quarles [37].

ponderomotive scaling [38] as given by

$$kT_{\mathrm{h}} \simeq m_{\mathrm{e}}c^2 \left[\sqrt{1 + \frac{I\lambda^2}{2.8 \times 10^{18}}} - 1 \right],$$

which results in a fast electron temperature of about 6.5 MeV for the average laser intensity $5 \times 10^{20}\,\mathrm{W\,cm^{-2}}$ used in the experiment. Measurements in previous experiments indicate [39, 40] a lower fast electron temperature between 1 and 2 MeV and conversion efficiencies between 40% and 50%. In fact, the way the fast electron temperature is derived from the average laser intensity in the focal spot area is not established. The low intensity tails of the laser intensity distribution in the target plane generate fast electrons with lower temperatures. The mean energy of the overall fast electron distribution will therefore be lower than the fast electron temperature calculated from the laser intensity in the (FWHM) focal spot area. It was shown that a more detailed analysis of the experimental results, performed with a sum of exponential fast electron distributions having a range of temperatures as retrieved from the ponderomotive scaling taking into account the actual laser intensity distribution in the focal spot, give a better agreement between the calculated bremsstrahlung spectrum and the experimental data [32]. The calculation of the actual local fast electron temperature from the laser intensity distribution in our experimental conditions using this procedure is now in progress.

As the Kα emission yield from the Cu tracer layer gives information about the fast electron temperature after the transport in the Al and the SiO_2 layer, respectively, propagation effects can account for a different fast electron temperature at the arrival in the Cu layer. From a purely collisional modelling of the electron stopping in the two different materials no significant differences are expected, as Al and SiO_2 have similar mean atomic number Z.

Other physical mechanism due to the lower resistivity of the metallic Al front layer with respect to the dielectric SiO_2 front layer might account for more efficient fast electron stopping in the dielectric target material. As a high-current fast electron beam propagates through matter,

a neutralizing counterpropagating return current will be set up. The return current must be coincident with the fast electron current within a collisionless skin depth c/ω_p otherwise the energy in the magnetic field would be greater than that available from the driving electron beam [3]. In dielectric materials such as SiO_2 no free electrons are available to form the return current. Therefore, ionization of the target atoms must occur at the front of the fast electron beam. Numerical results have shown that in dielectric targets field ionization occurs at the leading edge of the fast electron beam. These primary electrons acquire kinetic energy in the direction opposite to the fast electron beam and create secondary electrons via collisional ionization behind the ionization front. Energy losses due to this mechanism may be of the order of a few tens of per cent of the initial fast electron energy [11].

Nevertheless, from the graph in figure 7 it is clear that a different fast electron energy can account at most for the increase of a factor of 3 in the K shell ionization cross section, and thus, taking into account equation (1), results at most in the increase of a factor of 3 in the number of produced Kα photons, whereas in the experiment an enhancement of Kα emission by a factor of about 8 was measured. Therefore, propagation effects cannot completely explain the observed difference.

In contrast, the interaction conditions at the arrival of the main laser pulse for the SiO_2 target might differ significantly from those for the Al target due to different preplasma formations. In transparent materials such as SiO_2, linear absorption of the laser light is negligible and the onset of plasma formation depends on the presence of impurities or surface/volume defects in the material [41, 42]. The plasma formation threshold (around $10^{12}\,\mathrm{W\,cm^{-2}}$) is therefore much higher than in metals, e.g. in the case of an Al target, significant plasma formation was observed with a nanosecond prepulse with an intensity of $2 \times 10^9\,\mathrm{W\,cm^{-2}}$ [43]. In addition, vaporization of the target material can occur in metals at intensities as low as $10^8\,\mathrm{W\,cm^{-2}}$ [44]. Preplasma formation is therefore expected to start earlier during the rise of the ASE pedestal in Al than in SiO_2 and the plasma will expand to larger distances in the case of the Al target.

Clearly, the plasma density profile at the arrival of the main laser pulse affects the fast electron generation. Differences in the initial fast electron temperature can arise from a different electron density profile. In steeper density profiles the skin depth is reduced leading to less penetration of the electromagnetic fields and thus to less energetic fast electrons [1, 47]. Recent simulations have shown that depending on the preplasma scalelength, different scenarios can occur during the laser–plasma interaction [45]. In that paper, the short (long) density gradient case corresponds to a plasma of about 10 (25) μm size from near solid density to 0.1 of the critical density. Considering a plasma expansion velocity of $10^6\,\mathrm{cm\,s^{-1}}$, this corresponds to the onset of plasma formation at about 1 (2.5) ns before the arrival of the main pulse. The simulation results show that density profile steepening occurs around the relativistic critical density $\gamma_{os} n_c$, where n_c is the critical density and $\gamma_{os} = \sqrt{1 + a_0^2}$, and a low density shelf is formed in front of the target. For the short gradient case, the density step is larger and the density in the shelf in front of the target is lower, leading to lower fast electron energies than in the long density gradient case. Without entering into detail in the acceleration mechanism proposed in [45], we note here that laser absorption is found to decrease for the short gradient case in that paper. As pointed out in [45], this might be due to the 1D treatment, as in similar simulations accounting for 2D effects, higher and less density-dependent absorption was found [46]. The absorption behaviour is consistent with the fact that the number of fast electrons in the skin layer increases with the target density n as $n^{1/2}$, whereas the fast electron energy decreases as $n^{-1/2}$ [46].

Therefore, a steeper preplasma gradient in the case of the SiO_2 target can lead to a lower fast electron temperature and higher total number of fast electrons, roughly proportional to

the temperature decrease. Both the decrease in the electron energy and the higher number of electrons contribute to increase the transfer of energy, leading to an enhancement of the Kα radiation. Although a detailed analysis would be required for a quantitative modelling of our results, these circumstances already suggest that the observed differences in x-ray yield may be a consequence of the different vacuum–plasma interaction conditions.

6. Conclusions

We described an experimental investigation of fast electron energy deposition in interaction conditions relevant for the FI approach to inertial confinement fusion. Enhanced Kα emission generated by the crossing of fast electrons in the tracer layer after propagation in an SiO_2 layer was observed. It was shown that the high Kα yield cannot depend only on propagation effects and implies a higher number of fast electrons generated during the interaction. The different preplasma conditions generated by the ASE pedestal of the laser pulse on SiO_2 and Al targets and the effects of the different interaction conditions on the generated fast electron energy distribution and number was discussed.

In principle, the generation of a higher number of fast electrons with lower mean energy is a positive outcome for the FI approach to inertial confinement fusion, as the fast electron energy can be coupled more efficiently to the compressed core.

Acknowledgments

This work is part of the experimental validation programme of the European HiPER project on Inertial Confinement Fusion Energy. One of the authors (P K) acknowledges the COST P14 Action for financial support (STSM) for the participation at the experimental campaign at the VULCAN laser facility.

References

[1] Wilks S C and Kruer W L 1997 *IEEE J. Quantum Electron.* **33** 1954
[2] Salzmann D 2002 *Phys. Rev.* E **65** 056409
[3] Evans R G 2007 *Plasma Phys. Control. Fusion* **49** B87
[4] Schlegel Th *et al* 1999 *Phys. Rev.* E **60** 2209
[5] Honda M *et al* 2000 *Phys. Plasmas* **7** 1302
[6] Sentoku Y *et al* 2003 *Phys. Rev. Lett.* **90** 155001
[7] Davies J R 2003 *Phys. Rev.* E **68** 056404
[8] Mason R J *et al* 2005 *Phys. Rev.* E **72** 015401 (R)
[9] Kemp A J *et al* 2006 *Phys. Rev. Lett.* **97** 235001
[10] Bell A R *et al* 1997 *Plasma Phys. Control. Fusion* **39** 653
[11] Klimo O *et al* 2007 *Phys. Rev.* E **75** 016403
[12] Luther-Davies B *et al* 1987 *Phys. Rev.* A **35** 4306
[13] Beg F N *et al* 1997 *Phys. Plasmas* **4** 447
[14] Wharton K B *et al* 1998 *Phys. Rev. Lett.* **81** 822
[15] Pisani F *et al* 2000 *Phys. Rev.* E **62** R5927
[16] Batani D 2002 *Laser Part. Beams* **20** 321
[17] Hansen S B *et al* 2005 *Phys. Rev.* E **72** 036408
[18] Evans R G *et al* 2005 *Appl. Phys. Lett.* **86** 191505
[19] Theobald W *et al* 2006 *Phys. Plasmas* **13** 043102
[20] Gizzi L A *et al* 2007 *Plasma Phys. Control. Fusion* **49** B211
[21] Wei M S *et al* 2004 *Phys. Rev.* E **70** 056412
[22] Labate L *et al* 2007 *Appl. Phys.* B **86** 229
[23] Norreys P A *et al* 2006 *Plasma Phys. Control. Fusion* **48** L11

[24] Lancaster K L *et al* 2007 *Phys. Rev. Lett.* **98** 125002
[25] Santos J J *et al* 2002 *Phys. Rev. Lett.* **89** 025001
[26] Manclossi M *et al* 2006 *Phys. Rev. Lett.* **96** 125002
[27] MacKinnon A J *et al* 2001 *Phys. Rev. Lett.* **86** 1769
[28] Reich Ch *et al* 2000 *Phys. Rev. Lett.* **84** 4846
[29] Rose S J 2005 *Plasma Phys. Control. Fusion* **47** B735
[30] Key M H 2007 *Phys. Plasmas* **14** 055502
[31] Tabak M *et al* 1994 *Phys. Plasmas* **1** 1626
[32] Patel P 2008 *10th Int. Workshop on Fast Ignition of Fusion Targets* (Hersonissos, Crete, Greece, 12–18 June 2008)
[33] Scofield J H 1974 *Phys. Rev.* A **9** 1041
[34] Giulietti D and Gizzi L A 1998 *Riv. Nuovo Cimento* **21** 1
[35] Jackson J D 1975 *Classical Electrodynamics* 2nd edn (section 15.2) (New York: Wiley)
[36] Liu M *et al* 2000 *At. Data Nucl. Data Tables* **76** 213
[37] Quarles C A 1975 *Phys. Rev.* A **13** 1278
[38] Wilks S C *et al* 1992 *Phys. Rev. Lett.* **69** 1383
[39] Chen H *et al* 2005 *The 4th Int. Conf. on Inertial Confinement Fusion Science and Applications* (Biarritz, France)
[40] Yasuike K *et al* 2001 *Rev. Sci. Instrum.* **72** 1236
[41] Rethfeld B 2007 *Contrib. Plasma Phys.* **47** 360
[42] Gruzdev V E and Chen J K 2008 *Appl. Phys.* A **90** 255
[43] Boehly T R *et al* 2001 *Phys. Plasmas* **8** 231
[44] Wharton K B *et al* 2001 *Phys. Rev.* E **64** 025401 (R)
[45] Kemp A J *et al* 2008 *Phys. Rev. Lett.* **101** 075004
[46] Chrisman B *et al* 2008 *Phys. Plasmas* **15** 056309
[47] Denavit J 1992 *Phys. Rev. Lett.* **69** 3052